

Chemical Science



Accepted Manuscript

This article can be cited before page numbers have been issued, to do this please use: J. Zhang, A. Xu, C. Yang, X. Wu, H. Lin and Q. Zhu, *Chem. Sci.*, 2025, DOI: 10.1039/D5SC06905J.



This is an Accepted Manuscript, which has been through the Royal Society of Chemistry peer review process and has been accepted for publication.

Accepted Manuscripts are published online shortly after acceptance, before technical editing, formatting and proof reading. Using this free service, authors can make their results available to the community, in citable form, before we publish the edited article. We will replace this Accepted Manuscript with the edited and formatted Advance Article as soon as it is available.

You can find more information about Accepted Manuscripts in the <u>Information for Authors</u>.

Please note that technical editing may introduce minor changes to the text and/or graphics, which may alter content. The journal's standard <u>Terms & Conditions</u> and the <u>Ethical guidelines</u> still apply. In no event shall the Royal Society of Chemistry be held responsible for any errors or omissions in this Accepted Manuscript or any consequences arising from the use of any information it contains.



View Article Online DOI: 10.1039/D5SC06905J

Science Accepted Manuscrip

ARTICLE

Maximizing the Second-Harmonic Generation Response via Coordination-Induced Localization of Nonbonding Electrons

Received 00th January 20xx, Accepted 00th January 20xx

DOI: 10.1039/x0xx000000x

Jia-Xiang Zhang, a,b,c A-Lan Xu, a,b Yang Chi, *,d Xin-Tao Wu, a,b Hua Lin, *,a,b and Qi-Long Zhu*,a,b

To enhance laser frequency conversion efficiency, the development of nonlinear optical (NLO) crystals with strong second-harmonic generation (SHG) responses remains a central challenge. However, for chalcogenides, atomic-level crystal design has seldom yielded materials with SHG responses exceeding 3 × AgGaS₂. Previous studies suggest that modulation of nonbonding electrons can enhance both linear and NLO properties, yet strategies to localize nonbonding electrons for maximizing SHG remain underexplored. Here, we demonstrate that reducing the coordination number increases the spatial localization of nonbonding electrons, thereby boosting SHG performance. Guided by this principle, we synthesized KBiP₂S₆ (P2₁, no. 4), exhibiting the highest SHG response among sulfides to date (15 × AgGaS₂). Atomic space tessellating analysis reveals that ~75% of the SHG contribution originates from S, particularly from localized S-3p nonbonding electrons—challenging conventional stereochemically active lone-pair (SCALP)-based contribution models that overlook dominant role of S. Moreover, symmetry analysis identifies the polar screw axis as the favorable symmetry for high-SHG SCALP-based chalcogenides. This work transitions NLO material design from structural building-unit assembly to electronic-level engineering, opening new avenues for next-generation high-performance NLO materials.

Introduction

Second-harmonic generation (SHG), as one of the most prominent and widely applied nonlinear optical (NLO) effects, plays a critical role in laser frequency conversion. $^{1-3}$ Among the various factors influencing the frequency doubling process, conversion efficiency is paramount. The efficiency of SHG is largely governed by two key parameters: the magnitude of the effective nonlinear coefficient ($d_{\rm eff}$) and the ability to achieve phase matching (PM). These parameters directly determine whether a crystal can deliver efficient frequency-doubled laser output. Consequently, in the field of NLO crystals, there is an ongoing pursuit of materials that exhibit strong SHG responses while maintaining a balanced set of properties suitable for practical applications.

In the infrared (IR) region, one of the most critical challenges in the study of NLO chalcogenide crystals lies in the inherent trade-off between SHG response and band gap. ⁴⁻⁶

In tetrahedral units, sulfur atoms often adopt multiple coordination environments due to corner-sharing connections, transitioning from four-fold to three-fold, two-fold, or even mono-coordination.⁹ A decrease in coordination number leads to the degree of localization of nonbonding electrons on sulfur. The increased presence of nonbonding electrons near the valence band maximum (VBM) is favorable for enhancing

Crystals based on selenides and tellurides often exhibit strong SHG responses, but their practical applications are severely limited by their narrow band gaps, which lead to two-photon absorption and low laser induced damage threshold. Consequently, in the more promising sulfide-based systems, the central question that continues to attract intense research interest is: how to maximize the SHG response while avoiding a narrow band gap? This challenge is equally relevant in the ultraviolet-visible (UV-Vis) and deep-ultraviolet (DUV) regions. Previous studies have primarily focused on nonbonding electrons, where their role was analyzed within the context of symmetry. It was found that in polar tetrahedral units, the nonbonding electrons on anions exhibit favorable cooperative alignment under polar screw axes and $\overline{\mathbf{4}}$ axis symmetry. This alignment not only enhances the SHG response but also allows for modulation of the material's linear optical properties. This strategy led to the discovery of Mg₂PO₄Cl,⁷ a phosphate crystal with the strongest SHG response among DUV non- π conjugated systems, and [Ba₄Cl₂][CdGa₄S₁₀],⁸ a Cd-based infrared material exhibiting optimal overall performance. However, the full potential of nonbonding electrons in enhancing NLO properties remains far from fully realized.

^{a.} State Key Laboratory of Structural Chemistry, Fujian Institute of Research on the Structure of Matter, Chinese Academy of Sciences, Fuzhou 350002, China.

^{b.} Fujian Science & Technology Innovation Laboratory for Optoelectronic Information of China, Fuzhou, Fujian 350108, China.

^c School of Materials Science and Engineering, Peking University, Beijing 100871, China.

^{d.} School of Chemistry and Chemical Engineering, Qufu Normal University, Qufu 273165, China.

^{*}Corresponding Author(s): yang.chi@hotmail.com; linhua@fjirsm.ac.cn; olzhu@fjirsm.ac.cn.

Electronic Supplementary Information (ESI) available: Additional experimental and theory results, together with additional tables and figures.

This article is licensed under a Creative Commons Attribution 3.0 Unported Licence Open Access Article. Published on 17 November 2025. Downloaded on 11/19/2025 1:54:20 AM.

ARTICLE Journal Name

the compound's SHG response.¹⁰ Therefore, maximizing the localization of nonbonding electrons on sulfur can fully activate the deformability of S atoms, increase their polarizability under external electromagnetic fields, and ultimately enable the material to exhibit a strong SHG effect.

To maximize the localization of nonbonding electrons on sulfur, the following aspects are considered as primary goals in crystal design: (1) Coordination number: to ensure rational connectivity between structural units while maintaining the maximum density and localization of nonbonding electrons on S, sulfur atoms should predominantly adopt twofold coordination within the crystal structure. (2) Interstitial cations: the incorporation of interstitial cations offers an effective strategy to disrupt dense anionic frameworks, thereby increasing structural diversity. Moreover, the formation of highly ionic bonds associated with these cations can further enhance the localization of nonbonding electrons, potentially amplifying the material's NLO response. (3) Building unit composition: in the IR region, commonly used units include polar tetrahedral structural stereochemically active lone-pair (SCALP) units, and other distorted polyhedra. A framework composed solely of slightly distorted polar tetrahedra tends to form various cornersharing modes, which not only results in a high number of interconnected units but also makes it difficult to maintain predominantly two-fold-coordinated sulfur atoms. introduction of distorted polyhedra, which connect via facesharing in addition to corner- or edge-sharing, is also suboptimal. In contrast, SCALP units, characterized by large distortion and a tendency to connect via corner-sharing while spatially separating from each other, provide a promising alternative. 11 Therefore, a rational design strategy can be realized by constructing frameworks centered on SCALP units bridged by tetrahedral units. The next step involves the selection of appropriate elements from the periodic table. Previous studies have demonstrated that within a given group, increased covalence of M-S bond reduces the deformability of nonbonding electrons. As such, Pb2+ and Bi3+, which are heavy metals with strong lone-pair activity, are preferred as central atoms in SCALP units. 12 To ensure a sufficiently wide band gap, light elements from the second and third periods—such as Li+, Mg^{2+} , Al^{3+} , Si^{4+} , and P^{5+} —are considered as auxiliary cations. Excluding those likely to form six-fold coordination, only Si4+ and P5+ remain.13

After integrating the aforementioned crystal design principles, we refocused our research on the ABiP₂S₆ system, which had not been fully understood previously. 14,15 Earlier experiments demonstrated that RbBiP₂S₆ exhibited the highest SHG response among sulfides at the time (11.9 × benchmark AgGaS₂).¹⁴ However, under the traditional framework of anionic group theory, the deep connection between the high SHG response and the complex inorganic structure, especially systems with significant multi-atom interactions, remained unclear. To overcome this limitation,

we shifted our focus from a "group-centered" to an "atomcentered" perspective and quantitative Pplathally 22605616269FG contributions of each atom in the anionic group. This analysis revealed that, in KBiP₂S₆, approximately 75% of the SHG response originates from the coordinated sulfur atoms, rather than the traditionally emphasized central atom. This finding challenges the previous design paradigm, which placed primary focus on the central atom, and emphasizes the importance of modulating the local coordination environment of the Q2- anion through the central atom to enhance its polarizability. Guided by this revised structure-property relationship, we optimized the experimental measurements and successfully synthesized millimeter-level KBiP₂S6 crystals, which exhibited the highest SHG response among known sulfides (15 × benchmark AgGaS₂). This value significantly exceeds its previously reported performance,15 improving by a factor of 8.3. Not only does this result validate the effectiveness of our theoretical model, but it also suggests that the potential performance of some previously reported crystals has yet to be fully explored. To extend the applicability of this design strategy, we further statistically analyzed the spatial configurations and symmetry features of SCALP units. We found that polar helical axes, as an advantageous symmetry, can provide a strong theoretical basis for earlystage screening, aiding the structure prediction and exploration of high-performance NLO materials.

Results and Discussion

KBiP₂S₆ crystallizes in the non-centrosymmetric space group P2₁ (Table S1), with its high-symmetry axis aligned along the baxis in monoclinic system, corresponding to the direction of 21 screw axis. Due to the primitive lattice (P-lattice), the unit cell lacks atoms at body-centered and face-centered positions, and all atoms occupy general Wyckoff positions (2a), indicating the absence of high-symmetry crystallographic sites (Table S2). To simplify the coordination description of Bi, the strongly bonded Bi-S interactions (< 3.0 Å) were modeled as discrete [BiS₄] units (Table S3 and S4). These [BiS₄] units connect with [P₂S₆] groups via both corner-sharing and edge-sharing modes, forming composite [BiP2S7] units. These composite units further connect through corner-sharing along the 2₁-screw axis, generating one-dimensional chain-like structures (Figure 1). Interestingly, the distortion orientation of the [BiS₄] units along the local C2 axis is consistent with the direction of the 21screw axis in the crystal, resulting in a uniform alignment of the polar [BiS₄] units along the polar axis. This directional consistency favors constructive SHG response accumulation. Within this chain structure, most S atoms are two-fold coordinated, particularly those shared between [BiS4] and $[P_2S_6]$ units. However, S4 and S6 atoms from the $[P_2S_6]$ group exhibit mono-coordination, extending outward from the chains. This structural arrangement closely aligns with the original crystal design strategy, and the coherent alignment of

Open Access Article. Published on 17 November 2025. Downloaded on 11/19/2025 1:54:20 AM.

Journal Name ARTICLE

polar units along the polar axis provides a robust structural foundation for the observed strong SHG response.

View Article Online DOI: 10.1039/D5SC06905J

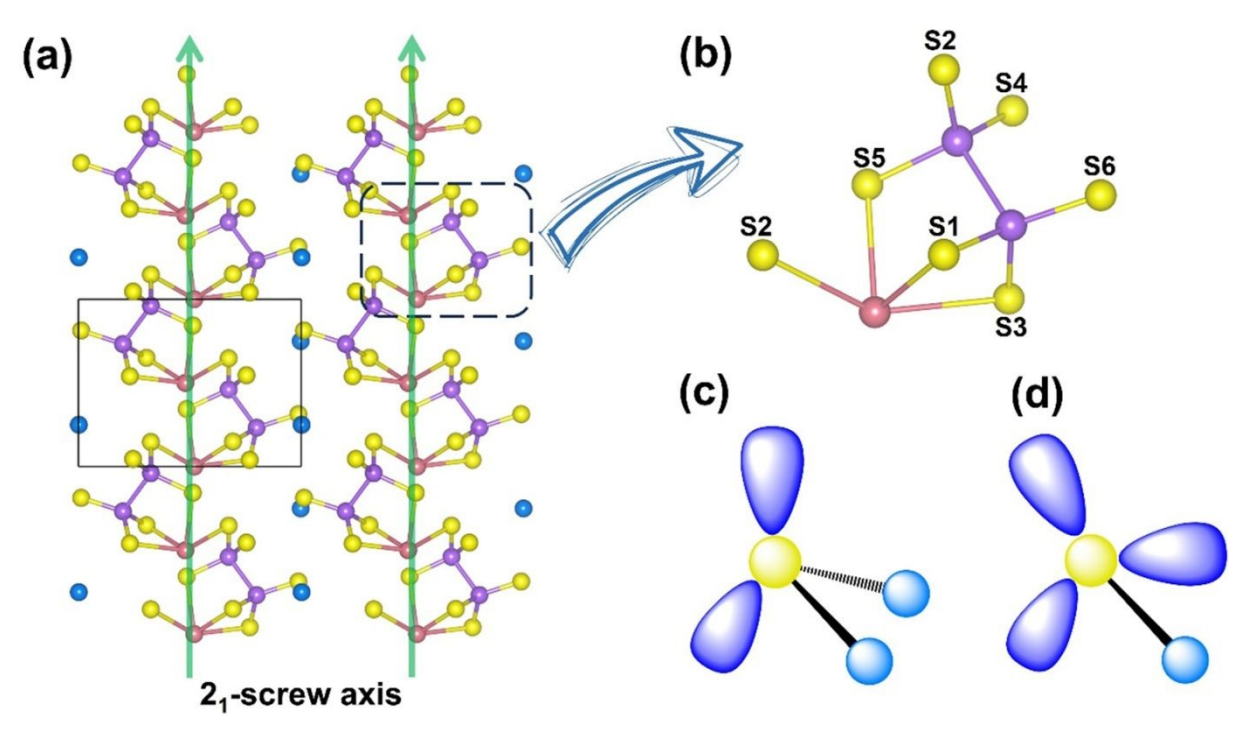


Figure 1. The structure of KBiP₂S₆: (a) the chain-like structure arranged around 2_1 -screw axis; (b) the minimum repeating units [BiP₂S₇], which composed by [BiS₄] and [P₂S₆]; the sketch of (c) two-coordinated S about S1, S2, S3, S5 and (d) mono-coordinated S about S4 and S6.

Energy-dispersive X-ray spectroscopy (EDX) (Figure S1) and powder X-ray diffraction (XRD) (Figure 2a) confirmed the phase purity of the compound. Thermal analysis indicated that the compound begins to decompose at 800 K (Figure S2). Further XRD analysis of the thermally treated sample revealed significant changes in peak intensities and the appearance of new diffraction peaks, supporting the thermal decomposition result (Figure S3). Diffuse reflectance spectroscopy performed on powder samples showed an optical band gap (Eg) of 2.24 eV, consistent with the observed red color of the crystals (Figure 2b). Furthermore, the LIDT of KBiP₂S₆ was evaluated employing the single-pulse method,16 yielding a value of 27.64 MW/cm2 at 1064 nm. This result is significantly higher than that of the benchmark material AgGaS₂ (2.82 MW/cm²) measured under the same conditions.¹⁷ IR transmission measurements on the single crystal, in conjunction with the reflectance data, revealed a broad transmission window ranging from 0.52 to 15.3 µm (Figure 2c). It is widely recognized that higher crystallinity correlates with fewer intrinsic defects, thereby more accurately reflecting a material's intrinsic optical properties. Our previous study on RbBiP₂S₆ revealed SHG response as high as 11.9 times that of AgGaS₂, ¹⁴ whereas other reports on its isostructural counterpart, KBiP₂S₆, ¹⁵ reported an SHG response of only 1.8 times AgGaS2. This significant disparity in performance, arising solely from the substitution of alkali metal cations, contradicts the widely accepted anionic group theory, which attributes NLO properties primarily to the

behavior of anionic structural units. In previous studies, the direct synthesis of KBiP₂S₆ crystals from elemental precursors often resulted in limited crystal quality and size, primarily due to the constraints of solid-solid reactions. 15 To overcome this challenge, we adopted an optimized synthesis route utilizing a boron-chalcogen synthesis method18, with KI added as a flux agent to improve both reaction activity and crystal quality. Powder SHG measurements employing the Kurtz-Perry technique were conducted to evaluate the SHG coefficient of KBiP₂S₆. Figure 2d demonstrates a distinct particle-size dependence of SHG intensity for KBiP₂S₆, where enhanced SHG responses with increasing particle size suggest phase-matching behavior. Remarkably, at a laser wavelength of 2050 nm, KBiP₂S₆ exhibits an SHG efficiency 15 times greater than that of $AgGaS_2$ within the particle size range of 150-210 μm . These results underscore the importance of evaluating crystallinity as a key factor in SHG measurements, especially for NLO crystal candidates. Furthermore, this insight suggests that previously reported NLO crystals with excellent structural features may exhibit even better performance if optimized for higher crystallinity. Moreover, a distinctive testing result was observed in the SHG measurements of KBiP₂S₆. Across the particle size range from small to large, the crystal consistently exhibited a strong SHG response. This behavior differs significantly from that of most compounds, which typically show a pronounced increase in SHG intensity with increasing particle size, eventually reaching a plateau. Calculation of the

Shemical Science Accepted Manuscrip

ARTICLE Journal Name

coherence length 19 revealed a value of only 4 μ m, which is smaller than the initial particle sizes used in the tests. As a result, in the highly crystalline sample, the SHG response showed no significant increase with particle size. This

combination of a short coherence length and valuerge SHG response offers promising potential for further investigation of KBiP $_2$ S₆ in ultrafast optics and SHG microscopy applications.

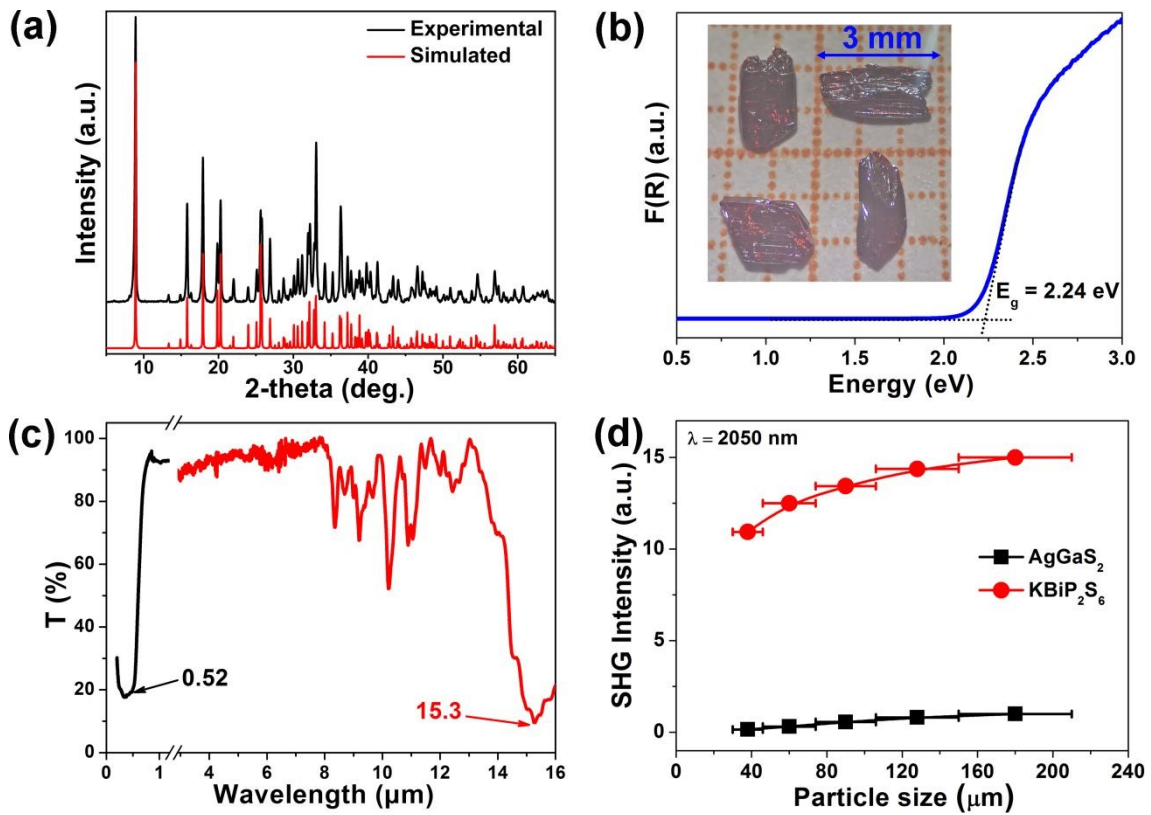


Figure 2. The characterization of KBiP₂S₆: (a) pure sample XRD pattern of KBiP₂S₆; (b) E_g of 2.24 eV with the correspondent 3 mm red block crystal; (c) optical transparent range from 0.52–15.3 μ m and (d) plots of powder SHG response versus particle size.

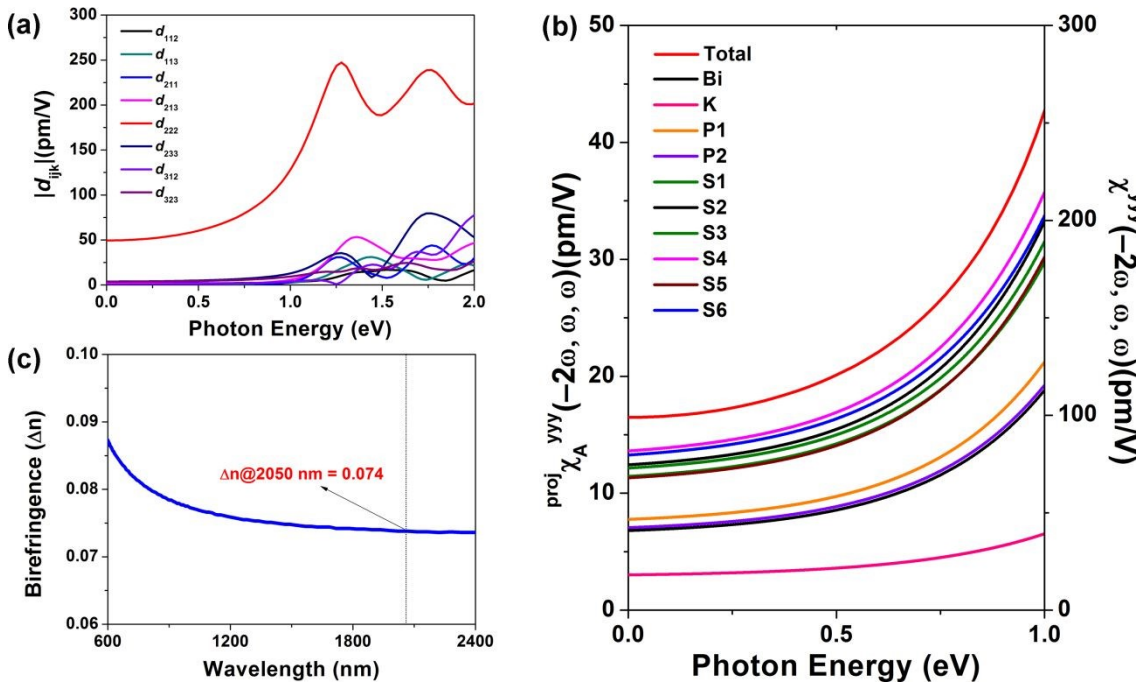


Figure 3. The linear and NLO calculation analysis of KBiP₂S₆: (a) the all eight non-zero d_{ijk} tensors, (b) the birefringence (Δn) at 2050 nm is 0.074 and (c) the second-order NLO polarizability and its projection onto different atoms in different energy of photoelectric field.

The structure-based predictions and experimental results confirm that the structure-property relationship of this compound aligns well with current theoretical models. To further investigate the individual contributions of each structural unit, we performed a detailed SHG response analysis of the compound using the AST method,²⁰ which is particularly suitable for evaluating contributions in systems containing SCALP units. Since KBiP₂S₆ crystallizes in the low-symmetry 2 point group, the Kleinman symmetry, 21 which is often used to simplify NLO tensor analysis, can significantly deviate in lowsymmetry compounds. Therefore, to ensure accuracy, all eight non-zero second-order NLO coefficients for this compound were calculated (Figure 3a). In the 0-1.0 eV incident photon energy range, all coefficients except d_{222} have nearly identical absolute values and contribute minimally to the overall response. However, beyond 1.0 eV, significant discrepancies arise among tensor components that would be considered equivalent under Kleinman symmetry. Overall, the effective SHG coefficient (d_{eff}) of KBiP₂S₆ is dominated by the d_{222} tensor component, and the macroscopic second-order polarization of the compound increases with rising incident photon energy (Figure 3b). Besides, its birefringence calculation results show that it has a birefringence of 0.074 at 2050 nm, which can effectively compensate for the phase mismatch caused by dispersion (Figure 3c).22

Compared to conventional static tensor analysis, the AST method offers a dynamic perspective, more accurately reflecting the induced dipole behavior of the material under an external optical field. Therefore, the contributions to the dominant d_{222} component were further traced. As shown in Table 1, under a 2050 nm laser field, S atoms contribute a remarkable 74.93%, whereas the combined contribution from Bi and P is only 22.19%, and K accounts for a minor 2.89%. If the analysis were conducted from the traditional functional group perspective, the contributions of the [BiS₄] and [P₂S₆] units would be 30.93% and 66.19%, respectively. This comparison clearly shows that the conventional approach significantly underestimates the role of S atoms in SHG activity. Attributing the significant contribution of S atoms solely to their associated structural units tends to shift researchers' focus toward the central elements, which may lead to a misinterpretation of the overall properties of the functional unit.

By visualizing the contribution of each atom in the form of diagrams, it is clearly observed that S atoms exhibit

significantly greater contributions than other elements across the 0-1 eV energy range. Through analysis using atomic spatial dipole component matrix maps, it was revealed that at 2050 nm (0.6 eV), the dipole moments of all atomic species in KBiP₂S₆ contribute positively to the macroscopic second-order nonlinear polarization (Figure 4a, the numerical data as Table S5 in the ESI). The dominant instantaneous dipole moments responsible for this response primarily arise from S-Bi, S-P, and S-S interactions, whereas transitions such as P-S, P-P, and S-K contribute to a similar but much lesser extent. This indicates that the key contributors to the SHG response are the transitions involving non-bonding electrons on S atoms concentrated near the valence band maximum (VBM). As previously discussed in the structural analysis, KBiP₂S₆ contains S atoms with two different coordination environments: twocoordinated S1, S2, S3, S5 and mono-coordinated S4 and S6. The diagram clearly shows that the most significant contributions to the polarization originate from transitions involving S4 and S6 to Bi. Additionally, transitions from S4 and S6 to K, P, and other sulfur atoms also exceed those of the two-coordinated sulfur atoms. In order to visualize the contributions of atoms on their VB and CB, further atomic SHG contributions were visualized at 0.6 eV (Figures 4b and 4c).

In addition to the contribution analysis at 0.6 eV, visualizations were also conducted at 0 eV and 1 eV (Figure S4 and S5). Combined with the projected density of states (PDOS), it is evident that the VB is primarily composed of S-3p and P-3p orbitals, while the conduction band (CB) is mainly derived from Bi-6p and S-3p orbitals (Figure 5a). This aligns well with the previously discussed transition contributions, confirming that the VBM is dominated by non-bonding S-3p states. Further supporting this, the PDOS curves of the two-coordinate S atoms (S4 and S6) and the mono-coordinate S atoms (S1-S3 and S5) clearly show that the S-3p states of the monocoordinate atoms possess higher non-bonding electron states near the VBM compared to the two-coordinate atoms (Figure 5c). This also strongly corroborates the view that monocoordinate S atoms have more non-bonding states, thereby inducing a larger microscopic contribution to the SHG (Figure 4a and Table 1). In oxide-based systems, 23-26 it has been suggested that the greater the activity of the s2 lone pair electrons on SCALP-type metal cations, the more significant their contribution to SHG. In the case of KBiP₂S₆, the VBM is not solely composed of Bi-6s orbitals but also includes contributions from Bi-6p orbitals.

This article is licensed under a Creative Commons Attribution 3.0 Unported Licence.

Open Access Article. Published on 17 November 2025. Downloaded on 11/19/2025 1:54:20 AM.

ARTICLE Journal Name

Table 1. The contribution percentage of each atom in atomic space to the SHG susceptibility d_{222} obtained using the AST, scheme. DOI: 10.1039/D5SC06905J at an incident wavelength of 2050 nm.

Atom	Contributions (%)	Atom	Contributions (%)
Bi	7.00	S2	12.61
K	2.89	S3	12.19
P1	7.95	S4	13.77
P2	7.24	S5	11.47
S1	11.59	S6	13.30

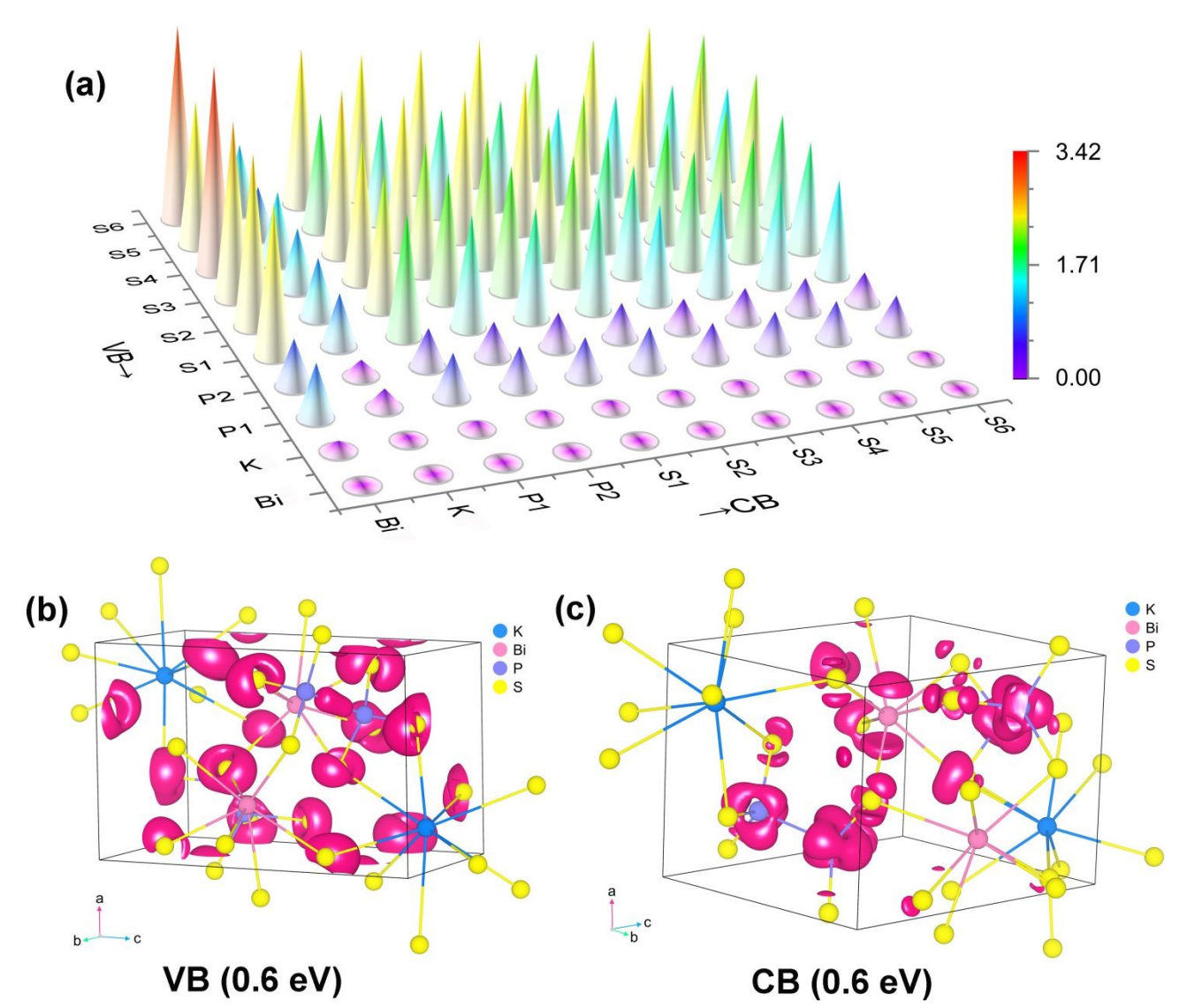


Figure 4. The origination analysis of SHG responses in KBiP₂S₆: (a) transition dipole moment component matrix diagram, and the SHG distribution functions in (b) VB and (c) CB at 0.6 eV (2050 nm)

When evaluating the s-orbital activity using the R_{sca} factor ²³ a value of 2.6 is obtained. If one were to overlook the differences in bonding strength between sulfides and oxides and directly apply the correlation between higher R_{sca} values and stronger SHG responses, then Bi in KBiP2S6 would be expected to contribute significantly to SHG. This appears to coincide with our experimental observations. However, PDOS calculations clearly demonstrate that the VBM in $KBiP_2S_6$ is

overwhelmingly dominated by non-bonding S-3p states, and that the contributions from Bi-6s and Bi-6p orbitals, as well as from their antibonding interactions with S, are negligible. In our earlier study of RbBiP₂S₆, static d_{222} tensor calculations showed that the VB-I region (-2.3 to 0 eV) plays a crucial role in the SHG response. This energy range corresponds to a region in KBiP₂S₆ where non-bonding S-3p states are highly concentrated and where nonbonding interactions between S

Journal Name ARTICLE

and Bi/P also reside (Figure 5b and S6). A similar conclusion has also been observed in nitrides. 27 Cheng et al. reported that in the MP₂N₄ (M = Ge, Sn, and Pb) series, the positive contribution of nonbonding states to the SHG response increases along the Ge-to-Pb substitution. Notably, only the Pb-based compound avoids the occurrence of negative SHG contributions that typically arise from overly strong bonding interactions, highlighting the beneficial role of weakly bound or nonbonding electrons in enhancing NLO performance. Evidently, the above contradictory result highlights the fundamental differences in bonding strength between oxide

and chalcogenide systems, underscoring the inadequacy of treating SCALP building units as unified 10 do in the 10 do in th

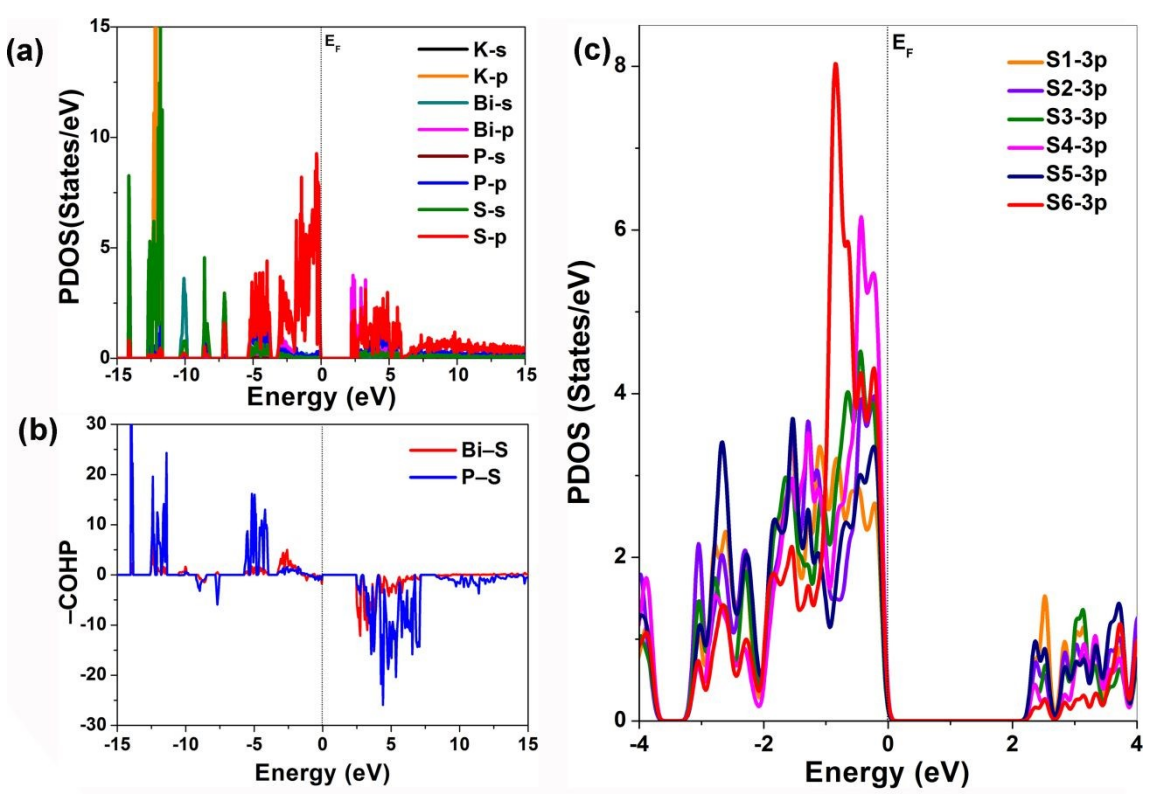


Figure 5. The SHG contribution analysis in SCALP units: (a) the PDOS of KBiP₂S₆, which shows the almost S-3p contribution in VBM; (b) the COHP analysis of total Bi–S and P–S bonds; (c) S-3p states of two-coordinate S atoms (S4 and S6) and the monocoordinate S atoms (S1-S3 and S5).

In contrast, such behavior is not observed in the sulfide $KBiP_2S_6$, providing further evidence that conclusions derived from oxide-based SCALP systems may not directly apply to their chalcogenide counterparts. In particular, the difference in atomic radii between oxygen and sulfur plays a critical role. The smaller radius of oxygen in oxides typically leads to structural units exhibiting SOJT distortions in octahedral environments with 3-, 4-, or 5-coordination. However, in sulfide systems, the larger atomic radius of sulfur introduces greater variability in bond lengths and coordination geometries, leading to distinct structural and electronic responses that must be considered independently from those of oxides.

Analysis of the Bi–S bond lengths in [BiS₄] unit reveals that the shorter Bi–S1 and Bi–S5 bonds (2.713 and 2.726 Å) experience stronger bonding interactions compared to the longer Bi–S2 and Bi–S3 bonds (2.806 and 2.898 Å). This

indicates a higher degree of covalency in the Bi-S1 and Bi-S5 bonds, which in turn leads to a reduced delocalization of the non-bonding electron density on S1 and S5. Consequently, S1 and S5 contribute less to the SHG response than S2 and S3, which could observed in S-3p PDOS. Within the [P2S6] unit, the strong covalent nature of the internal P-S bonds results in a relatively narrow bond length distribution (2.030-2.071 Å) for P-S1, S2, S3, and S5, indicating minimal variation in bonding strength. Even the bond lengths involving the singly coordinated sulfur atoms S4 and S6 are only slightly shortened to 1.988 and 1.967 Å, respectively. These subtle changes are insufficient to significantly strengthen the binding of the nonbonding electrons on S4 and S6, thereby allowing a higher degree of nonbonding electrons localization. As a result, S4 and S6 exhibit markedly stronger SHG contributions. Compared to their bi-coordinated counterparts, monocoordinated S atoms possess more nonbonding valence

Journal Name

ARTICLE

electrons. This results in higher chemical activity and enhanced deformability of their electron clouds under external optical fields. Physically, the d_{222} tensor component corresponds to the interaction of two optical electric fields polarized along the b-axis with the crystal, generating a nonlinear dipole oscillation that is also aligned with the b direction. Consequently, a stronger alignment of an S atom's electron cloud with the b-axis leads to a greater induced polarization. In KBiP₂S₆, the electron clouds of both mono- and bi-coordinated S atoms are predominantly oriented along the b direction, which explains the structure's large SHG response. Furthermore, differences in bond lengths and angles due to the distinct bonding

environments of S inevitably alter their electronic cloud orientations, thereby leading to their district contributions to the overall SHG effect. These structure—property correlation insights, supported by theoretical calculations, validate our design strategy centered on increasing the localization degree of nonbonding electrons on sulfur atoms. S atoms with lower coordination numbers are shown to contribute more significantly to the SHG response. Furthermore, this analysis underscores the limitations of treating the SCALP building unit as unified contributor in chalcogenides, suggesting that a more nuanced approach is required for accurate evaluation of NLO performance.

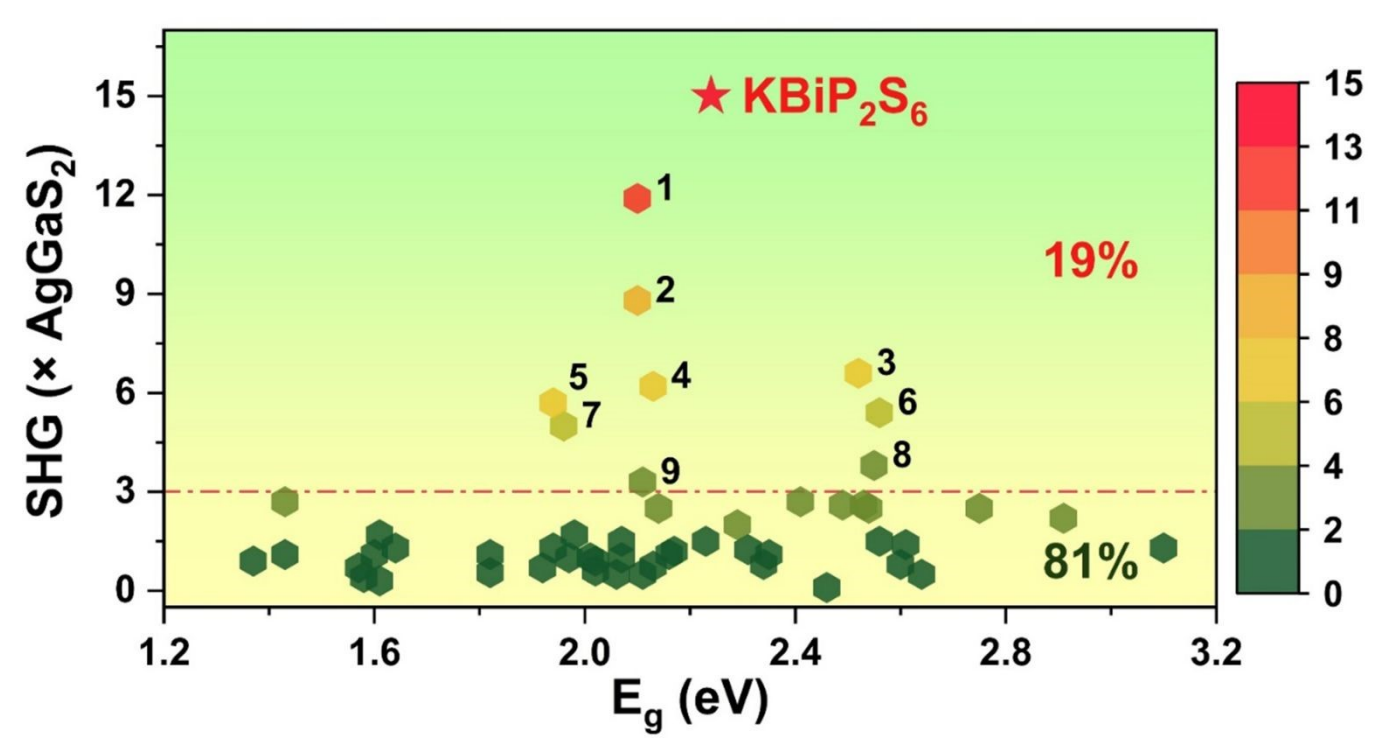


Figure 6. The statistical analysis of 53 SCALP-based chalcogenide compounds. The dashed line shows the SHG responses of 3 time of AgGaS₂.1: RbBiP₂S₆, 2: Hg₃AsSe₄I, 3: Na₆Sn₃P₄S₁₆, 4: Hg₃AsSe₄Br, 5: SbSI, 6: NaPb₃P₄S₁₆, 7: PbGa₂GeSe₆, 8: SnGa₄Se₇ and 9: PbGa₄Se₇.

A statistical analysis of the currently known 53 PM SCALPbased chalcogenides (Table S6) shows that they can be categorized by the group of the central SCALP atom—namely groups 14, 15, and 16 (Figure 6). Using a SHG efficiency of 3×AgGaS₂ as a performance threshold, only 10 compounds surpass this value, including PbGa₄Se₇ (Pc, 3.3×AgGaS₂),²⁹ SnGa₄Se₇ (Pc, 3.8×AgGaS₂), ³⁰ PbGa₂GeSe₆ (Fdd2, $5\times AgGaS_2$), ³¹ NaPb₃P₄S₁₆ (R3m, 5.4×AgGaS₂), ³² SbSI (Pna2₁, 5.7×AgGaS₂), ³³ Hg₃AsSe₄Br (*P*6₃*mc*, 6.2×AgGaS₂), ³⁴ Na₆Sn₃P₄S₁₆ $(R3m, 6.6 \times AgGaS_2)$, 35 Hg_3AsSe_4I $(P6_3mc, 8.8 \times AgGaS_2)$, 34 RbBiP₂S₆ ($P2_1$, 11.9×AgGaS₂)¹⁴ and KBiP₂S₆ ($P2_1$, 15×AgGaS₂). Except for SbSI, the remaining nine compounds are all constructed by combining tetrahedral units with SCALP units. In our previous studies, we identified that tetrahedral units preferentially adopt symmetry elements such as polar screw axes and fourfold roto-inversion axes. This raises the question

of whether SCALP units also exhibit similar symmetry Structural analysis of these nine highperformance SHG compounds reveals that, except for SnGa₄Se₇ and PbGa₄Se₇ which crystallize in the Pc space group, the others all crystallize in polar space groups containing screw axes: $Pna2_1$ (2₁), Fdd2 (2₁), R3m (3₁ or 3₂), and $P6_3mc$ (6₃). For SCALP units possessing SOJT activity, distortions along the C_2 , C_3 , or C_4 axes reduce the original O_h symmetry of ideal octahedra to lower point groups such as D_{2d} , C_{3v} , or C_{4v} . Further distortion from ideal configurations arises due to variations in coordination environments. Because of the significant distortion inherent to SCALP units, their crystallization in non-centrosymmetric space groups typically gives rise to a net dipole moment, externally manifesting as structures in polar space groups. These space groups often contain rotational axes and mirror planes, which-combined

This article is licensed under a Creative Commons Attribution 3.0 Unported Licence.

Open Access Article. Published on 17 November 2025. Downloaded on 11/19/2025 1:54:20 AM.

Journal Name ARTICLE

with translational symmetry—form screw axes and glide planes. The presence of screw axes implies an axial alignment of SCALP units within the crystal, which can occur in two forms: (1) The central element of the SCALP unit occupies a symmetry site on the screw axis, yielding a standard unit geometry with D_{2d} , C_{3v} , or C_{4v} symmetry. The corresponding screw axes are 2-, 3- (or 6₃-), and 4-fold, and this scenario ensures consistent stacking along the axis; (2) The SCALP units are helically arranged around the screw axis, leading to distorted geometries. In this case, the uniformity in stacking is reflected by the axial components of their dipole moments. Naturally, due to the flexible coordination number of SCALP units, their coordination environments are not limited to strong 3-, 4-, or 5-coordination; weaker bonding interactions may result in coordination numbers. Therefore, advantageous alignment of SCALP units within crystals will require further exploration of how different structural units induce orientation preferences in SCALP motifs. This constitutes a key direction for future research.

Conclusions

This article is licensed under a Creative Commons Attribution 3.0 Unported Licence

Open Access Article. Published on 17 November 2025. Downloaded on 11/19/2025 1:54:20 AM.

In this work, we revisited the ABiP₂S₆ system, which had not been fully understood in the context of previous crystal design principles. RbBiP₂S₆, previously reported as having the highest SHG response among sulfides (11.9 × AgGaS₂), exhibited a strong response but lacked a deep structural explanation under the conventional anionic group theory, particularly in systems with significant multi-atom cooperation. To overcome this limitation, we shifted from a "group-centered" to an "atom-centered" approach, quantitatively analyzing the SHG contributions of each atom within the anionic groups. Our findings revealed that in KBiP₂S₆, approximately 75% of the SHG response originates from the coordinated sulfur atoms, rather than the central atom traditionally emphasized. This challenges the previous design focus on central atoms and underscores the importance of controlling the coordination environment of Q2- anions to enhance their polarizability. Based on this structure-property relationship, we synthesized millimeter-level KBiP₂S₆ crystals, which exhibit the highest SHG response reported for sulfides to date (15 ×AgGaS₂), Eg of 2.24 eV, a high LIDT (9.8 × AgGaS₂ @1064 nm), a wide transmission window ranging from 0.52 to 15.3 μm , and a Δn of 0.074. This not only validates the proposed design model but also suggests that the full potential of some previously reported crystals may still be unexplored. Additionally, by analyzing the spatial configurations and symmetry features of SCALP units, we identified polar helical axes as a promising symmetry motif, providing a theoretical tool for early-stage screening and discovery of high-performance NLO materials.

Author contributions

View Article Online DOI: 10.1039/D5SC06905

Jia-Xiang Zhang: Investigation, Formal analysis, Writing-original

A-Lan Xu: Formal analysis.

Yang Chi: Methodology, Validation, Writing-review & editing. Xin-Tao Wu: Conceptualization, Writing-review & editing.

Hua Lin: Supervision, Conceptualization, Writing-review & editing.

Qi-Long Zhu: Supervision, Writing-review & editing.

Conflicts of interest

There are no conflicts to declare.

Data availability

All supplementary data for the results of this study are available in the article and its Electronic Supplementary Information (ESI) file.

Acknowledgements

This work was supported by the National Natural Science Foundation of China (22175175 and 22305142), Fujian Science & Technology Innovation Laboratory for Optoelectronic Information of China (2021ZR118), and the Youth Innovation Promotion Association CAS (2022303). The authors thank Prof. Bing-Xuan Li at FJIRSM for helping with the NLO measurements.

Notes and references

- (a) M. Mutailipu and S. Pan, Angew. Chem. Int. Ed., 2020, 59, 20302-20317. (b) M. Mutailipu, Z. H. Yang and S. L. Pan, Acc. Mater. Res., 2021, 2, 282-291. (c) Y. Q. Li, J. H. Luo and S. G. Zhao, Acc. Chem. Res., 2022, 55, 3460-3469.
- (a) J. Chen, C. L. Hu, F. Kong and J. G. Mao, Acc. Chem. Res., 2021, 54, 2775-2783. (b) H. Fan, N. Ye and M. Luo, Acc. Chem. Res., 2023, 56, 3099-3109. (c) B. Znang, M.-Y. Ran, X.-T. Wu, H. Lin and Q.-L. Zhu, Coord. Chem. Rev., 2024, 517, 216053. (d) W. Zhang, X. Hou, S. Han and S. Pan, Coord. Chem. Rev., 2024, 505, 215664.
- (a) H. Lin, W.-B. Wei, H. Chen, X.-T. Wu and Q.-L. Zhu, Coord. Chem. Rev., 2020, 406, 213150. (b) X. Liu, Y.-C. Yang, M.-Y. Li, L. Chen and L.-M. Wu, Chem. Soc. Rev., 2023, 52, 8699-8720. (c) W. Zhou and S.-P. Guo, Acc. Chem. Res., 2024, 57, 648-660. (d) P. Feng, J.-X. Zhang, M.-Y. Ran, X.-T. Wu, H. Lin and Q.-L. Zhu, Chem. Sci., 2024, 15, 5869-5896.
- (a) L. Kang, M. Zhou, J. Yao, Z. Lin, Y. Wu and C. Chen, J. Am. Chem. Soc., 2015, 137, 13049-13059. (b) W. F. Zhou, J. J. Wu, W. L. Liu and S. P. Guo, Coord. Chem. Rev., 2023, 477, 214950. (c) J.-X. Zhang, P. Feng, M.-Y. Ran, X.-T. Wu, H. Lin and Q.-L. Zhu, Coord. Chem. Rev., 2024, 502, 215617.
- (a) K. Wu and S. L. Pan, Coord. Chem. Rev., 2018, 377, 191-208. (b) H. Chen, M.-Y. Ran, W.-B. Wei, X.-T. Wu, H. Lin and Q.-L. Zhu, Coord. Chem. Rev., 2022, 470, 214706. (c) H.-D. Yang, M.-Y. Ran, W.-B. Wei, X.-T. Wu, H. Lin and Q.-L. Zhu, Mater. Today Phys., 2023, 35, 101127. (d) J. Huang, A. Abudurusuli, Z. Yang, S. Pan, Small, 2025, 21, 2409997.

Science Accepted Man

- (a) L. Gao, J. Huang, S. Guo, Z. Yang and S. Pan, Coord. Chem. Rev., 2020, 421, 213379.
 (b) M.-Y. Ran, A-Y. Wang, W.-B. Wei, X.-T. Wu, H. Lin and Q.-L. Zhu, Coord. Chem. Rev., 2023, 481, 215059.
 (c) H. Wang, M. Mutailipu, Z. Yang, S. Pan, J. Li, Angew. Chem. Int. Ed., 2025, 64, e202420526.
- 7 J.-X. Zhang, Q.-G. Yue, S.-H. Zhou, X.-T. Wu, H. Lin and Q.-L. Zhu, Angew. Chem. Int. Ed., 2024, 63, e202413276.
- J.-X. Zhang, S.-H. Zhou, X.-T. Wu, H. Lin and Q.-L. Zhu, *Angew. Chem. Int. Ed.*, 2025, **64**, e202506658.
- 9 (a) W. Wang, D. Mei, F. Liang, J. Zhao, Y. Wu and Z. Lin, Coord. Chem. Rev., 2020, 421, 213444. (b) J. Dang, D. Mei, Y. Wu and Z. Lin, Coord. Chem. Rev., 2021, 431, 213692. (c) H. Chen, W.-B. Wei, H. Lin and X.-T. Wu, Coord. Chem. Rev., 2021, 448, 214154.
- 10 (a) Y. Guo, F. Liang, J. Yao, Z. Lin, W. Yin, Y. Wu and C. Chen, *Inorg. Chem.*, 2018, **57**, 6795–6798. (b) M.-Y. Li, B.-X. Li, H. Lin, Y.-F. Shi, Z. Ma, L.-M. Wu, X.-T. Wu and Q.-L. Zhu, *Inorg. Chem.*, 2018, **57**, 8730–8734. (c) L. Kang, F. Liang, X. Jiang, Z. Lin and C. Chen, *Acc. Chem. Res.*, 2020, **53**, 209–217.
- 11 (a) M. Yan, H.-G. Xue and S.-P. Guo, Cryst. Growth Des., 2020, 21, 698–720. (b) H. Chen, X.-T. Wu and H. Lin, Coord. Chem. Rev., 2026, 547, 217123.
- (a) I. Chung, J. H. Song, J. I. Jang, A. J. Freeman, J. B. Ketterson, M. G. Kanatzidis, *J. Am. Chem. Soc.*, 2009, 131, 2647–2656. (b) W. F. Chen, B. W. Liu, S. M. Pei, X. M. Jiang, G. C. Guo, *Adv. Sci.*, 2023, 10, 2207630. (c) A-Y. Wang, S.-H. Zhou, M.-Y. Ran, B. Li, X.-T. Wu, H. Lin, Q.-L. Zhu, *Inorg. Chem. Front.*, 2024, 11, 3744–3754. (d) B. M. Oxley, J.-H. Lim, K.-H. Lee, J.-B. Cho, S. Sarker, J. Nag, M. J. Waters, J. M. Rondinelli, V. Gopalan, J. I. Jang, M. G. Kanatzidis, *Chem. Mater.*, 2025, 37, 2592–2602.
- (a) M.-Y. Li, Z. Ma, B.-X. Li, X.-T. Wu, H. Lin and Q.-L. Zhu, *Chem. Mater.*, 2020, **32**, 4331–4339. (b) Z. Li, J. Yao and Y. Wu, Cryst. Growth Des., 2020, 20, 7550–7564. (c) B.-J. Song, Z. Ma, B. Li, X.-T. Wu, H. Lin and Q.-L. Zhu, *Inorg. Chem.*, 2021, **60**, 4357–4361. (d) Z.-X. Chen, W. Liu and S.-P. Guo, *Coord. Chem. Rev.*, 2022, **474**, 214870. (e) Y. Kong, G. Zheng, Y. Du, J. Li and S. Pan, *Coord. Chem. Rev.*, 2025, **533**, 216514.
- 14 M.-M. Chen, S.-H. Zhou, W. Wei, M.-Y. Ran, B. Li, X.-T. Wu, H. Lin and Q.-L. Zhu, ACS Materials Lett., 2022, 4, 1264–1269.
- 15 V. Nguyen, B. Ji, K. Wu, B. Zhang and J. Wang, *Chem. Sci.*, 2022, **13**, 2640-2648.
- 16 M. J. Zhang, X. M. Jiang, L. J. Zhou and G. C. Guo, *J. Mater. Chem. C*, 2013, **1**, 4754.
- 17 (a) H. Chen, Y. Y. Li, B. X. Li, P. F. Liu, H. Lin, Q. L. Zhu and X. T. Wu, Chem. Mater., 2020, 32, 8012. (b) M. Y. Ran, S. H. Zhou, B. X. Li, W. B. Wei, X. T. Wu, H. Lin and Q. L. Zhu, Chem. Mater., 2022, 34, 3853. (c) M. Y. Ran, S. H. Zhou, B. X. Li, X. T.

- Wu, H. Lin and Q. L. Zhu, *Chem. Mater.*, 2024, 36, 11996–12005.

 DOI: 10.1039/DSSC06905J
- 18 (a) M.-M. Chen, S.-H. Zhou, W.-B. Wei, X.-T. Wu, H. Lin and Q.-L. Zhu, Adv. Optical Mater., 2022, 10, 2102123. (b) H. Chen, M.-Y. Ran, S.-H. Zhou, X.-T. Wu and H. Lin, Adv. Optical Mater., 2024, 12, 2401100. (c) P. Feng, S.-H. Zhou, B.-X. Li, J.-X. Zhang, M.-Y. Ran, X.-T. Wu, H. Lin and Q.-L. Zhu, ACS Appl. Mater. Interfaces, 2024, 16, 52682–52691.
- 19 R. W. Boyd, Nonlinear Optics, Elsevier: San Diego, United States, 2020.3
- 20 Y. Chi, J. Mater. Chem. C, 2025, 13, 3978-3987.
- 21 D. A. Kleinman, Phys. Rev., 1962, 126, 1977-1979.
- 22 (a) B. Znang, S.-H. Zhou, B.-X. Li, X.-T. Wu, H. Lin and Q.-L. Zhu, Chem. Sci., 2025, 16, 3218–3227. (b) J.-X. Zhang, M.-Y. Ran, A-Y. Wang, Z. Ma, X.-T. Wu, H. Lin and Q.-L. Zhu, ACS Materials Lett., 2025, 7, 1512–1519. (c) A-L. Xu, M.-Y. Ran, X.-T. Wu, H. Lin and Q.-L. Zhu, Coord. Chem. Rev., 2025, 540, 216775.
- 23 C. Hu, M. Mutailipu, Y. Wang, F. Guo, Z. Yang and S. Pan, Phys. Chem. Chem. Phys., 2017, 19, 25270–25276.
- 24 Q.-C. Song, C.-L. Hu, F. Kong and J.-G. Mao, *Angew. Chem. Int. Ed.*, 2025, **64**, e202424053.
- 25 M.-Q. Lin, C.-L. Hu, M.-F. Duan, B.-X. Li, J.-G. Mao and B.-P. Yang, *Angew. Chem. Int. Ed.*, 2025, **64**, e202504673.
- 26 Y. Hu, C. Wu, X. Jiang, Z. Wang, Z. Huang, Z. Lin, X. Long, M. G. Humphrey and C. Zhang, J. Am. Chem. Soc., 2021, 143, 12455–12459.
- X. Cheng, V. Trinquet, B. Ding, G.-M. Rignanese, X. Gonze and S. Deng, *Chem. Mater.*, 2025, **37**, 3709–3719.
- 28 J. Zhou, Q. Wu, A. Ji, Z. Jia and M. Xia, *Coord. Chem. Rev.*, 2025, **524**, 216332.
- 29 Z. X. Zheng, Z. X. Qiu, C. H. Xie, Y. P. Zhang, X. M. Jiang, B. W. Liu and G. C. Guo, *Sci. China Mater.*, 2023, **66**, 2795–2802.
- 30 Z.-Z. Luo, C.-S. Lin, H.-H. Cui, W.-L. Zhang, H. Zhang, Z.-Z. He and W.-D. Cheng, Chem. Mater., 2014, 26, 2743–2749.
- 31 Z.-Z. Luo, C.-S. Lin, H.-H. Cui, W.-L. Zhang, H. Zhang, H. Chen, Z.-Z. He and W.-D. Cheng, *Chem. Mater.*, 2015, **27**, 914–922.
- 32 C. Zhao, D. Lu, X. Tian, J. Xu, B. Zhang, K. Wu, H. Yu and H. Zhang, *Inorg. Chem.*, 2023, **62**, 21487–21496.
- 33 Y. Zhou, L.-T. Jiang, X.-M. Jiang, B.-W. Liu and G.-C. Guo, *Chin. Chem. Lett.*, 2025, **36**, 109740.
- 34 J. Chen, C. Lin, X. Jiang, G. Yang, M. Luo, X. Zhao, B. Li, G. Peng, N. Ye, Z. Hu, J. Wang and Y. Wu, *Mater. Horiz.*, 2023, 10, 2876–2882.
- 35 C. Zhao, B. Zhang, X. Tian, G. Zhou, J. Xu and K. Wu, *Inorg. Chem. Front.*, 2023, **10**, 5726–5733.

Open Access Article. Published on 17 November 2025. Downloaded on 11/19/2025 1:54:20 AM.

This article is licensed under a Creative Commons Attribution 3.0 Unported Licence.

All supplementary data for the results of this study are available in the article and its Electronic Supplementary Information (ESI) file.